RSC Advances

PAPER

View Article Online
View Journal | View Issue

Cite this: *RSC Adv.*, 2025, **15**, 34417

Enhancing the electrochemical performance of rGO-based ternary composite for next generation supercapacitors

Nirosha James,[a] Abhirami Krishna,[a] Amala Shaliya Joseph[b] and Sreeja P. B. *[a]

Received 26th July 2025
Accepted 13th September 2025

DOI: 10.1039/d5ra05408g

rsc.li/rsc-advances

This work explores the rational design and synthesis of a high-performance ternary nanocomposite rGO/CeO_2/PPy, by incorporating cerium oxide and polypyrrole into the rGO matrix, through a hybrid approach of combining hydrothermal synthesis with *in situ* oxidative polymerization. Comprehensive structural characterization of the rGO/CeO_2/PPy composite confirms the successful integration of components, revealing a hierarchically porous architecture that optimizes both charge transport and ion diffusion kinetics. The ternary composite exhibits exceptional interfacial interactions, including π–π conjugation between rGO and PPy, coupled with electrostatic stabilization from CeO_2, resulting in enhanced mechanical integrity and improved electrolyte accessibility. Electrochemical characterization reveals remarkable performance metrics, with a specific capacitance of 874 F g^{-1} and outstanding cyclic durability of 94% capacity retention after 5000 charge–discharge cycles at 1 A g^{-1}. The configured rGO/CeO_2/PPy//AC system exhibits exceptional energy storage performance, yielding an energy density of 39.6 Wh kg^{-1} while sustaining a power density of 2859 W kg^{-1}. These outstanding characteristics underscore the material's suitability as a cutting-edge electrode for sophisticated energy storage systems, showcasing the benefits of strategic component integration in hybrid nanocomposite design.

1. Introduction

The global energy landscape of the 21st century faces unprecedented challenges, driving extensive research into advanced energy storage technologies that can effectively harness clean and renewable energy sources.[1] Among these emerging solutions, supercapacitors (SCs) have been explored as an upcoming class of energy storage devices.[2,3] Their remarkable combination of exceptional power density, extended cycle stability, rapid charge–discharge capabilities, broad operational temperature tolerance, and environmental sustainability has positioned them at the forefront of energy storage innovations.[4]

Carbonaceous nanostructures have established themselves as paradigm-shifting materials for electrochemical energy storage applications.[5] Advanced carbonaceous materials, such as graphene, carbon nanotubes, nano fibers, and porous activated carbon, are widely integrated into electrical double-layer capacitors (EDLCs), wherein energy storage manifests *via* electrostatic charge aggregation at the electrode–electrolyte interface.[6] In contrast, pseudocapacitive materials, including transition metal oxides, chalcogenides, and conductive polymers, rely on reversible faradaic reactions to achieve higher energy densities.[7] To harness the complementary strengths of both mechanisms, hybrid supercapacitors have been engineered, integrating electric double-layer capacitive and pseudocapacitive materials to optimize overall electrochemical performance.[8]

The dimensionality of the nanocarbon architectures plays a pivotal role in determining their physicochemical properties, with classifications ranging from 3D structures to 0D systems.[9] Among the multidimensional carbon architectures, two-dimensional (2D) carbon-based materials, particularly reduced graphene oxide, provide unparalleled advantages for electrochemical energy storage owing to their sheet-like structure with ultrahigh theoretical surface area (~2630 m^2 g^{-1}), mechanical stability, and exceptional electrical conductivity.[10] However, the practical realization of these properties is significantly hindered by the spontaneous restacking of graphene layers through strong π–π interactions.[11] To address this fundamental limitation, the strategic insertion of spacer materials between rGO sheets becomes essential to maintain optimal interlayer separation and prevent recombination.[12] Combining rGO with pseudocapacitive materials through covalent or noncovalent interactions enables the emergence of synergistic properties beyond those of individual components.[13,14]

The versatility of multivalent transition metal oxides makes them highly appealing for supercapacitors due to their potential for multiple oxidation state transitions, which facilitates enhanced pseudocapacitive behavior.[15]

---

[a] *Department of Chemistry, Centre for Renewable Energy and Environmental Sustainability, CHRIST University, Bengaluru 560029, India*

[b] *Inorganic and Bioinorganic Research Laboratory, Department of Chemistry, NIT Calicut, India. E-mail: sreeja.pb@christuniversity.in*

Among the various metal oxides, ceria (CeO_2) has garnered significant attention due to its pivotal role in advancing environmental and energy-related technologies. A key attribute of ceria is its ability to undergo rapid and reversible redox transitions between Ce^{3+} and Ce^{4+} oxidation states, a property that has been exploited in supercapacitor applications.[16] However, despite its redox versatility, the widespread adoption of CeO_2 in supercapacitor systems has been constrained by its inherently low electrical conductivity.[17] This limitation restricts charge storage primarily to surface reactions, leaving the bulk of the material electrochemically inactive and thus diminishing its overall capacitive performance. To circumvent this challenge, researchers have increasingly turned to conductive carbon matrices as structural scaffolds for the incorporation of metal oxides in the composite electrodes.[18] The incorporation of transition metal oxides into rGO frameworks serves to inhibit the π–π stacking tendency of graphitic layers while establishing a highly accessible, redox-active interface.[19]

A synergistic approach combining nanostructured carbon matrices and metal oxides with conductive polymers presents a compelling strategy to harness the advantages of both pseudocapacitive and electric double-layer charge storage mechanisms.[20] This sophisticated integration capitalizes on the unique benefits of each component: the substantial conductivity and extensive surface area of graphene derivatives, the rich redox chemistry of metal oxides, and the high charge density of conducting polymers.[21] Together, they form composite materials with optimized electrochemical properties that surpass the performance of their individual constituents, offering new possibilities for advanced energy storage solutions.

Jayaweera *et al.* made a significant contribution to this domain by designing rGO/SnO_2/PANI nanocomposite, synthesized through a scalable one-pot process.[22] This ternary composite exhibited reliable capacitance (524.2 F g^{-1}) under extreme cycling conditions. Moreover, Murat *et al.* developed an economically viable rGO/ZnO/PTh hybrid composite *via* chemical synthesis using $FeCl_3$ as an oxidant. It showcased an impressive C_{sp} of 430 F g^{-1}, with retaining near-constant capacitance across 1000 operational cycles.[23] Additionally, Jose *et al.* showcased the development of an innovative rGO/PdO/PPy ternary nanocomposite through straightforward electrodeposition, achieving a capacitance of 595 F g^{-1} and retaining 88% capacitance in 1 M H_2SO_4. The strategic design of ternary composites has emerged as a highly effective approach to engineer novel materials with superior electrochemical properties.

This study demonstrates the synthesis of a hybrid ternary composite rGO/CeO_2/PPy, incorporating reduced graphene oxide (rGO), cerium oxide (CeO_2), and polypyrrole (PPy), through a facile hydrothermal method with subsequent *in situ* chemical oxidative polymerization. It is anticipated that the synergistic combination of conductive rGO, redox-active CeO_2, and pseudocapacitive PPy prevents graphene restacking while improving charge transfer and ion diffusion kinetics. The distinctive structure of the composite optimizes ion diffusion channels and enhances capacitance, yielding exceptional cycling robustness and rate capability. The study provides a strategic blueprint for designing advanced energy storage systems through synergistic material engineering.

2. Experimental techniques

2.1 Materials

Cerium nitrate hexahydrate ($Ce(NO_3)_3\cdot 6H_2O$), Sodium hydroxide pellets (NaOH), pyrrole (Py), ferric chloride hexahydrate ($FeCl_3\cdot 6H_2O$) (Sigma-Aldrich). Polyvinylidene difluoride (PVDF), *N*-methyl-2-pyrrolidone (NMP), and carbon black (Kailash Scientific, India). Double-distilled water was employed throughout the experiments.

2.1.1 Synthesis of preparation of rGO/CeO_2 binary composite (RC). The rGO/CeO_2 nanocomposites were synthesized *via* a facile hydrothermal approach. Initially, GO (0.04 g) was uniformly dispersed in 30 mL of distilled water under ultrasonication for 60 min. Subsequently, 0.08 g cerium nitrate was introduced under continuous magnetic stirring for 30 min to ensure homogeneous mixing. 20 mL of 2 M NaOH solution was added, and the stirring was further continued. It was then subjected to a hydrothermal process at 180 °C for 12 h. The resultant black precipitate was centrifuged and washed to remove the unwanted residues. The purified product was dried overnight in a hot air oven at 70 °C to yield the final nanocomposite rGO/CeO_2.

2.1.2 Preparation of rGO/PPy binary composite (RP). The rGO/PPy nanocomposite was synthesized through an optimized *in situ* chemical oxidative polymerization process. Initially, 0.04 g of rGO was exfoliated in 30 mL of deionized water *via* probe ultrasonication for 60 min. To this dispersion, 0.2 M freshly distilled pyrrole monomer was introduced under constant stirring at 0–5 °C for 1 h to ensure proper monomer adsorption on the rGO sheets. Polymerization was subsequently initiated by dropwise addition of 0.2 M $FeCl_3$ oxidant solution, with the reaction proceeding under continuous magnetic stirring for 24 h. The obtained product was purified through subsequent washing and finally vacuum dried at 70 °C to obtain the conductive rGO/PPy composite.

2.1.3 Preparation of rGO/CeO_2/PPy ternary composite (RCP). The rGO/CeO_2/PPy ternary composite was synthesized through an integrated two-stage synthesis protocol combining the hydrothermal method and *in situ* oxidative polymerization as depicted in Fig. 1.

2.1.4 Characterizations. The crystallinity and structural properties of the samples were investigated using a Rigaku Miniflex 600-benchtop powder X-ray diffractometer. The identification of major surface functional groups within the materials was detected by employing the Shimadzu FTIR-8400S spectrophotometer. The morphological features and elemental composition were characterized using a Nova Nano SEM 450 instrument and a Thermo Fisher Scientific Tecnai G220 S-TWIN TEM analyzer. To examine the material composition and bonding interactions, a PHI5000 probe III instrument was employed. The surface area characteristics and porosity of the materials were assessed using a Micromeritics 3 Flex instrument. The electrochemical performance was comprehensively evaluated using a CHI6054E electrochemical workstation.

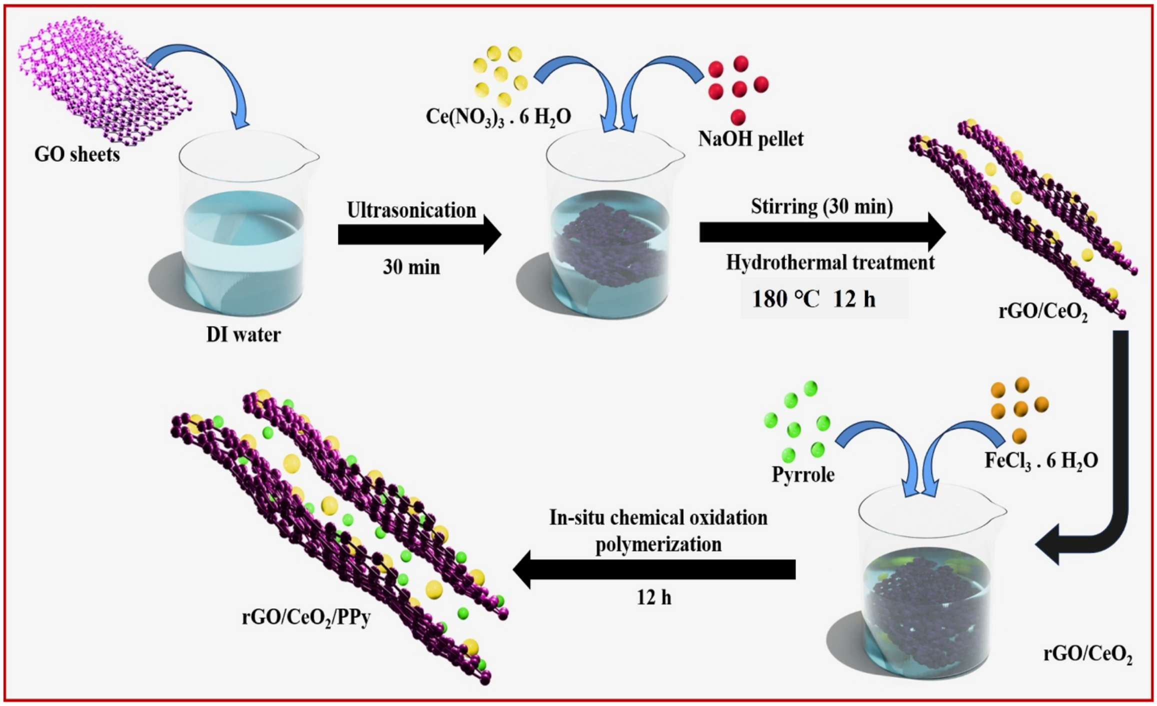

Fig. 1 Schematic illustration of the synthesis of rGO/CeO$_2$/PPy (RCP) ternary composite.

2.1.5 Preparation of rGO/CeO$_2$/PPy electrodes. The synthesized rGO/CeO$_2$/PPy ternary composite was homogenized with PVDF binder and conductive carbon black (8 : 1 : 1 mass ratio) in *N*-methyl-2-pyrrolidone (NMP) *via* rigorous stirring for 2 h. The resulting slurry was uniformly coated onto a nickel foam substrate (1 × 1 cm^2) and vacuum-dried at 60 °C for 12 h to ensure optimal adhesion and solvent removal. Electrochemical assessments were done using a Pt counter electrode and an Ag/AgCl (saturated KCl) reference electrode in 2M KOH. The CHI608E workstation was employed to conduct cyclic voltammetry (CV), galvanostatic charge–discharge (GCD), and electrochemical impedance spectroscopy (EIS) techniques to probe capacitive behavior, charge storage kinetics, and interfacial resistance, respectively.

The specific capacitance (C_{sp}) of the materials can be calculated from GCD curves using the following equation.

$$C_{sp} = \frac{I \times \Delta t}{m \times \Delta V} \tag{1}$$

2.1.6 Fabrication of rGO/CeO$_2$/PPy//AC asymmetric supercapacitor. A novel solid-state hybrid supercapacitor device was engineered by integrating rGO/CeO$_2$/PPy composite (RCP) as the battery-type positive electrode and activated carbon (AC) as the capacitive-type negative electrode, separated by a Whatman filter paper membrane immersed in the electrolyte, assembled in a two-electrode cell configuration. The electrochemical performance was rigorously assessed through an integrated analytical approach employing CV, GCD, and EIS, complemented by comprehensive stability evaluations. Comprehensive electrochemical characterization revealed optimal device operation over the potential window 0 to 1.4 V.

The energy storage capabilities were quantitatively assessed by calculating the energy density (*E*) and power density (*P*) parameters from the GCD profiles using the following standard equations:

$$E = \frac{C_{sp} \times V^2}{7.2} \tag{2}$$

$$P = \frac{E}{t} \times 3600 \tag{3}$$

3. Results and discussions

3.1 Structural characterizations

X-ray diffraction (XRD) analysis was used to assess the phase purity and crystallinity of the composites (Fig. 2). Fig. 2a shows the XRD patterns of pristine CeO$_2$, GO, and PPy. CeO$_2$ exhibits sharp Bragg peaks at 2θ values of 28.4° (111), 32.9° (200), 47.3° (220), 56.1° (311), 58.8° (222), 69.3° (400), 76.5° (331), and 78.9° (420), matching the face-centered cubic fluorite structure (JCPDS 65-2975).[24] Moreover, GO displays peaks at 10.8° (001) and 42.3° (100), while PPy shows a broad peak at 24.8°, reflecting its amorphous nature.[25,26] In RC and RP composites, CeO$_2$ and PPy peaks persist, but rGO peaks are absent due to GO reduction and uniform CeO$_2$ dispersion, disrupting graphitic stacking. The ternary RCP composite's XRD pattern reveals overlapping contributions from rGO, CeO$_2$, and PPy, confirming hybridization. Slight CeO$_2$ peak shifts indicate interfacial

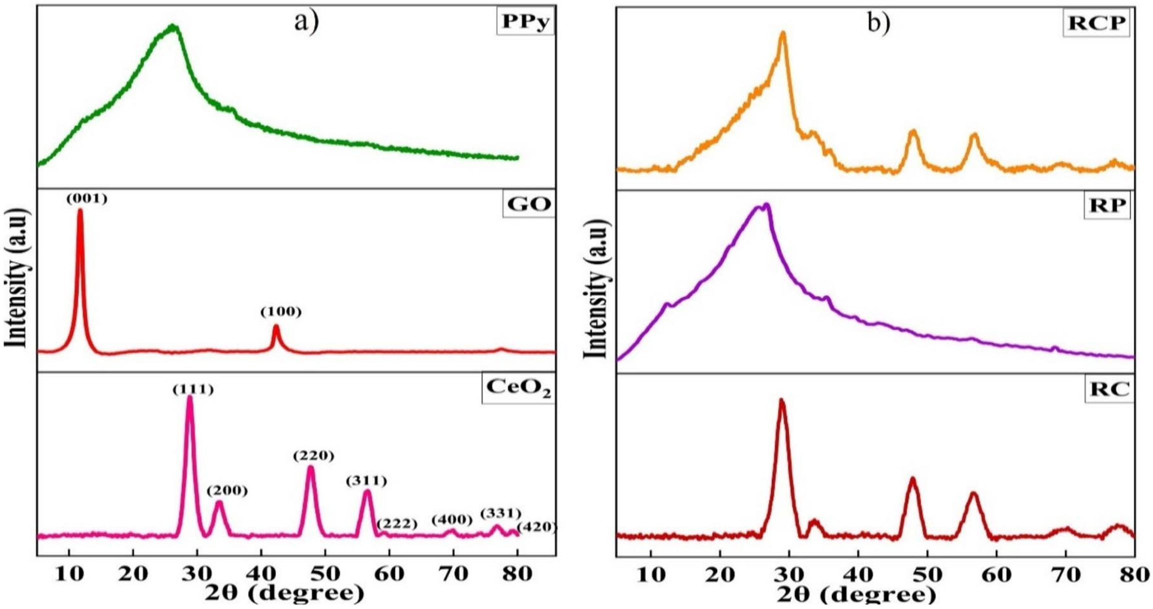

Fig. 2 The XRD pattern obtained for (a) CeO_2, GO, PPy; (b) RC, RP, and RCP.

interactions, preserving crystalline integrity and forming a synergistic structure ideal for electrochemical applications.

Raman spectroscopy offers critical insights into the structural and intermolecular dynamics of the nanocomposite system (Fig. 3).[27] The CeO_2 spectrum shows a distinct peak at 460 cm^{-1}, linked to symmetric Ce–O bond stretching in the fluorite structure, clearly visible in the RC composite, confirming ceria incorporation.[28] Graphene oxide displays characteristic D (1354 cm^{-1}) and G (1584 cm^{-1}) bands, arising from disordered sp^3 carbon and in-plane vibrations of sp^2 hybridized carbon atoms, respectively, which persist in the RC composite alongside the CeO_2 peak, indicating structural integrity and material integration.[29] The PPy spectrum reveals key vibrational signatures: G-band at 1557 cm^{-1} (C═C stretching), D-band at 1378 cm^{-1} (pyrrole ring deformations), and peaks at 1054 cm^{-1} (C–H bending) and 954 cm^{-1} (quinoid structures), reflecting electronic and structural changes in the conjugated backbone.[30,31] These features are prominent in the RP and RCP composites, confirming effective PPy integration with rGO and CeO_2, validating a well-integrated ternary nanocomposite system.

The I_D/I_G ratio in Raman spectroscopy is a key indicator of disorder in carbonaceous materials, with higher ratios reflecting increased structural defects. For graphene oxide (GO) and polypyrrole (PPy), the I_D/I_G ratios were measured as 0.98 and 0.72, respectively. The binary composite RC exhibited an I_D/I_G

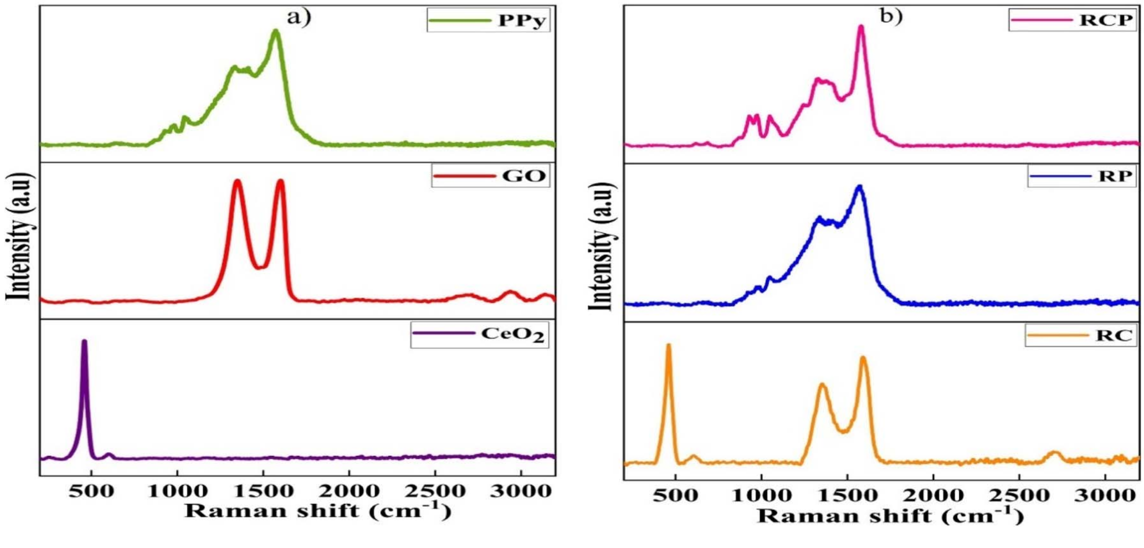

Fig. 3 Raman spectra obtained for (a) CeO_2, GO, PPy; (b) RC, RP, and RCP.

ratio of 0.89, suggesting a partial restoration of sp^2 domains in GO due to the removal of oxygen-containing defect states during reduction. In the hydrothermal reduction of GO to reduced graphene oxide (rGO), oxygen functional groups are eliminated, reestablishing the conjugated graphene network.[32] In the RCP composite, Raman spectra showed the same characteristic peaks as PPy, but with an increased I_D/I_G ratio from 0.72 to 0.79, indicating structural disruption in PPy due to oxygen-containing groups. This disruption may result from the incorporation of cerium particles into the pores of PPy.[33]

FTIR spectroscopy provides essential molecular insights into the functional group composition of synthesized materials (Fig. 4). The CeO_2 spectrum shows a prominent Ce–O vibrational mode at 485 cm^{-1}, retained in RC and RCP composites, confirming ceria nanoparticle integration.[34] Surface-adsorbed CO_2 is evidenced by peaks at 1328 cm^{-1} (O–C–O asymmetric stretching) and 1056 cm^{-1} (C═O stretching), while broad bands at 1524 cm^{-1} (hydroxyl bending) and 3428 cm^{-1} (O–H stretching) indicate surface hydration.[35,36] Graphene oxide (GO) exhibits peaks at 1720 cm^{-1} (carbonyl C═O), 1390 cm^{-1} (epoxy C–O–C), 1118 cm^{-1} (hydroxyl C–OH), and 1051 cm^{-1} (epoxide), with vibrations at 1289 cm^{-1} (C–O), cm^{-1} (aromatic C═C), and 1789 cm^{-1} (carbonyl C═O) in composites, suggesting partial GO reduction while preserving oxygen functionalities for enhanced electrochemical activity.[37,38] The FT-IR spectrum of PPy displays bands at 1552 cm^{-1} (C═C stretching), 1470 cm^{-1} (C–N stretching), 1042 cm^{-1} (N–H deformation), and 1174 cm^{-1} (pyrrole ring breathing), confirming its conjugated structure.[39] The RCP composite's combined vibrational features validate the successful integration of CeO_2, PPy, and carbonaceous material.

The surface properties of nanostructured materials significantly impact their electrochemical performance, as analyzed *via* N_2 physisorption using Brunauer–Emmett–Teller (BET) theory. The RCP ternary composite displays a type IV isotherm with distinct hysteresis loops at $P/P_0 > 0.4$, indicating a well-developed mesoporous structure conducive to efficient mass transport through capillary condensation (Fig. 5a).[40] Moreover, the pore size distribution curves of the materials determined by the Barrett–Joyner–Halenda (BJH) model are displayed in Fig. 5b.[41] It clearly indicates that most of the pores in the materials lie between 10 and 50 nm, emphasizing the mesoporous nature of the materials. The mesoporous materials serve as an unhindered ion transport pathway, facilitating the charge transfer kinetics. It provides more active sites for electrochemical reactions, improves the conductivity of the composite, and thereby enhances the overall electrochemical performance of RCP.[42] The BET-specific surface area of 85.8 m^2 g^{-1} reflects the synergistic integration of rGO nanosheets, CeO_2 nanoparticles, and PPy globules into a 3D framework, enhancing electrochemically active sites and electrolyte accessibility for superior charge transfer kinetics in energy storage applications.[43]

X-ray photoelectron spectroscopy (XPS) was employed to characterize the chemical states and bonding configurations within the synthesized hybrid material, revealing precise electronic properties and interfacial interactions at the atomic level.[44] The survey spectrum of the composite showcased in Fig. 6a represents four sharp peaks at 285.32 eV, 400.13 eV, 532.1 eV, and 900.7 eV corresponding to C 1s (69.25%), N 1s (10.48%), O1s (18.38%), and Ce 3d (1.89%), respectively. The Ce 3d was deconvoluted into six Gaussian components representing trivalent and tetravalent states of cerium ions (Fig. 6b). The peaks at 898.4 eV and 917.4 eV represented two spin orbitals of Ce 3d$_{3/2}$ and Ce 3d$_{5/2}$ of the Ce^{4+} state, respectively.[45] The Ce^{3+} oxidation state was represented by the peaks at 901 eV (Ce 3d$_{5/2}$) and 883.41 eV (Ce 3d$_{3/2}$). In addition to this, two satellite peaks were also found with binding energies of 907.5 eV and 888.6 eV.

The area under the peaks corresponding to each oxidation state was calculated from the fitted curves using Casa XPS software, and the ratio of Ce^{3+} (40.09%) to Ce^{4+} (18.34%) was obtained as 2.18. The XPS spectrum of CeO_2 reveals the ratio of Ce^{3+} and Ce^{4+} on its surface, which is directly linked to the concentration of oxygen vacancies.[46] A higher Ce^{3+} concentration indicates more oxygen vacancies, increasing the number of

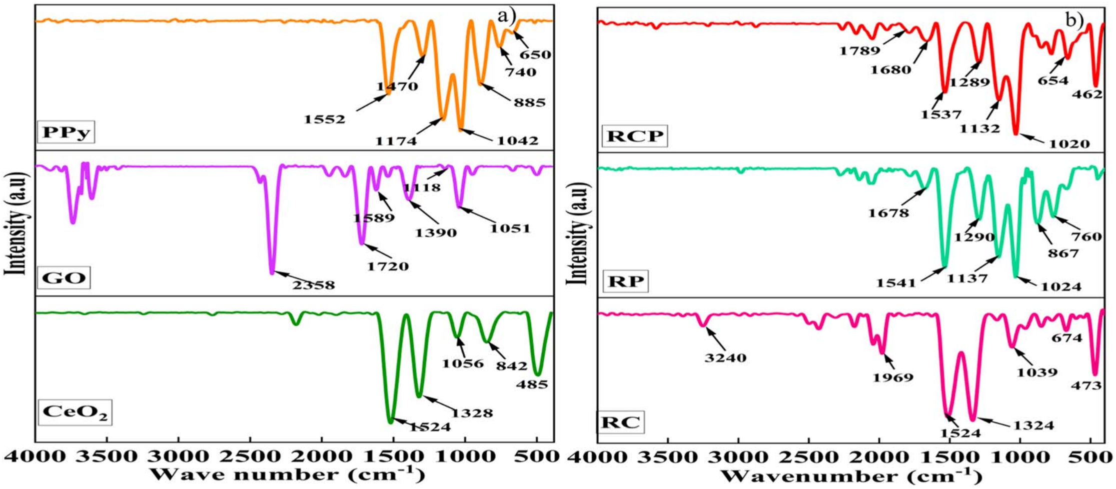

Fig. 4 FTIR spectra obtained for (a) CeO_2, GO, and PPy; (b) RC, RP, and RCP.

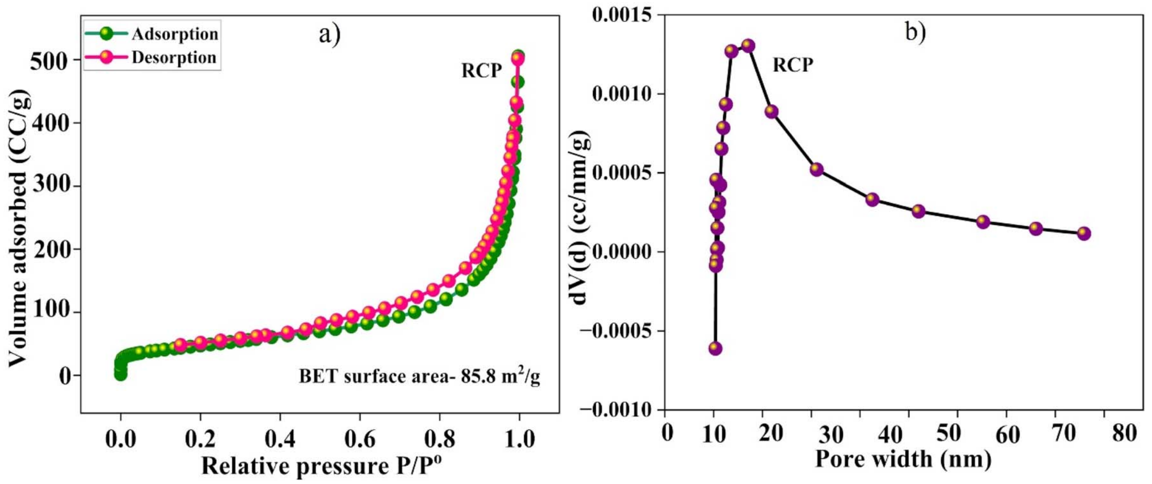

Fig. 5 (a) The BET curve of RCP (b), the pore size distribution curve of RCP.

active sites available for redox reactions and providing high-diffusivity pathways for electrolyte ions, leading to higher specific capacitance and improved energy storage capabilities.[47] Moreover, the presence of Ce^{3+}ions, with their single unpaired 4f electron, introduces donor energy levels in the CeO_2 band gap. This creates conductive electron transfer channels that enhance the material's overall electrical conductivity.[48] This is a key reason for creating composites with conductive materials like graphene.

As illustrated in Fig. 6c, the C 1s peaks at 284.7 eV, 286.2 eV, and 288.5 eV could be attributed to the alkyl C–C and sp^2 bonded C═C moieties, C–O of hydroxyl and epoxy groups, or C–N of pyrrole ring and carbonyl C═O groups present in the polypyrrole and rGO.[49] The N 1s core level spectrum of the composite consisted of two components, represented by 397.5 eV corresponding to the imine (═N–) nitrogen atoms, and 399.9 eV, which could be assigned to the neutral nitrogen (–N–H) in the pyrrole ring (Fig. 6d).[50] The high-resolution O 1s spectrum showed two fitted peaks corresponding to lattice oxygen ($O_{lattice}$ at 530.3 eV), corresponding to the oxygen atoms in the crystal lattice, and another peak corresponding to the adsorbed oxygen (O_{ads} at 532.8 eV), representing the active oxygen moieties at the surface (Fig. 6e).[51]

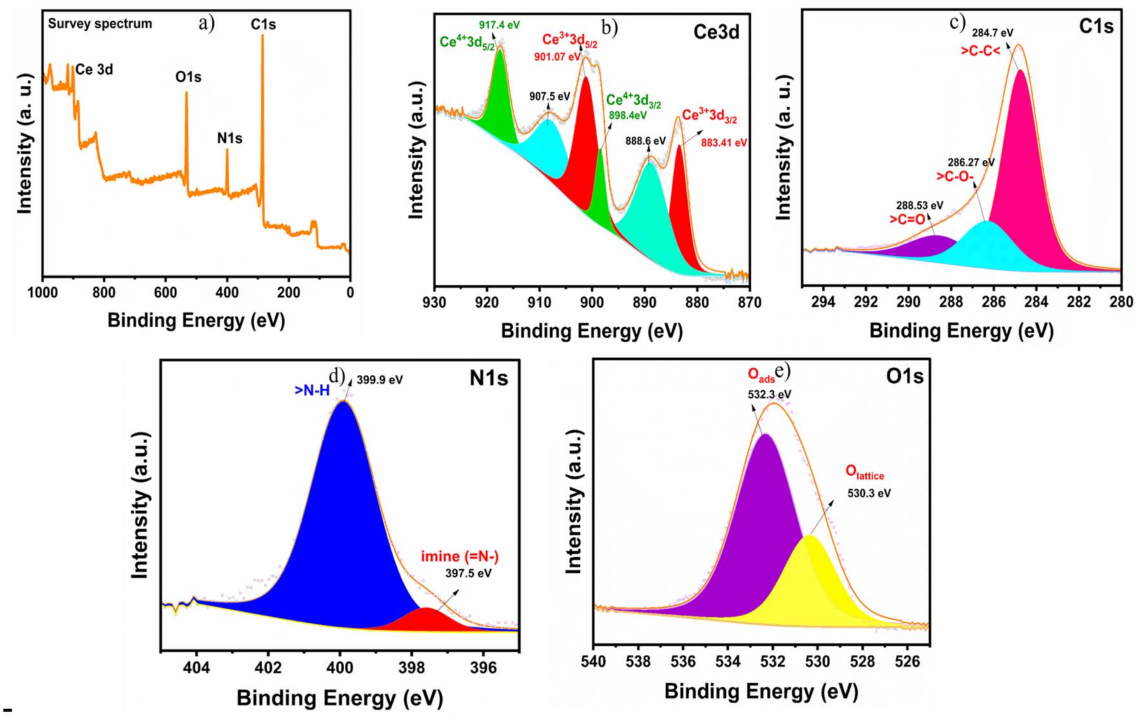

Fig. 6 (a) The survey spectra of RCP, deconvoluted peaks of (b) Ce 3d, (c) C 1s, (d) N 1s, (e) O 1s.

3.2 Morphological characterization

Field Emission Scanning Electron Microscopy (FESEM) was used to examine the surface morphology and microstructure of RC, RP, and RCP composites.[52] The FESEM image of RC (Fig. 7a) shows CeO_2 nanoparticles uniformly anchored on rGO sheets, indicating strong interfacial interactions and effective nucleation, enhancing electron transport and structural stability. Fig. 7b reveals the homogeneous coverage of spherical PPy particles on rGO, which is attributed to strong π–π interactions between PPy and graphene sheets, which inhibit restacking of rGO and facilitate the formation of a porous architecture.[53] The SEM image of the RCP ternary composite (Fig. 7c) displays rectangular CeO_2 and PPy spheres integrated into rGO, acting as spacers to create voids and gaps, fostering a 3D framework that supports rapid ion diffusion and redox reactions. Energy Dispersive X-ray (EDX) analysis of RCP (Fig. 7d) confirms the presence of carbon, nitrogen, cerium, and oxygen, verifying the formation of a well-integrated rGO/CeO_2/PPy hybrid system, where each component retains its chemical identity while synergistically enhancing the composite's functional properties.[54]

High-resolution transmission electron microscopy (HRTEM) and selected area electron diffraction (SAED) were used to investigate the crystallinity and nanostructure of the ternary RCP composite, as shown in Fig. 8a–d.[55] HRTEM images at various magnifications reveal uniformly distributed square-shaped CeO_2 nanocubes within the rGO-PPy matrix, consistent with SEM findings. This strong interfacial integration indicates effective heterostructure formation, crucial for synergistic electrochemical performance.[56] HRTEM images display clear lattice fringes with interlayer spacings of 0.27 nm and 0.31 nm, corresponding to the (200) and (111) planes of cubic CeO_2, confirming high crystallinity and phase purity of CeO_2 nanoparticles (Fig. 8c).[57] These results align with XRD and XPS data, verifying successful component integration while maintaining crystallographic integrity. The SEAD patterns demonstrate the coexistence of crystalline diffraction spots from CeO_2 and diffuse rings from amorphous PPy (Fig. 8d).[58] The well-defined heterostructure, with intimate interfacial contact between constituents, suggests enhanced charge transport capabilities, critical for advanced energy storage applications.[59]

3.3 Electrochemical analysis

The electrochemical investigations of the synthesized materials were done using various analytical techniques such as CV, GCD, and EIS. The Cyclic voltammetry (CV) was carried out in 2 M KOH within a potential window of -0.2 to 0.7 V to investigate the charge storage mechanism of the fabricated electrodes. CV curves of RC, RP, and RCP were recorded at scan rates ranging from 5 to 100 mV s^{-1} (Fig. 9), highlighting the relationship between applied potential and current response. The CV curves of all materials exhibited well-defined reduction and oxidation

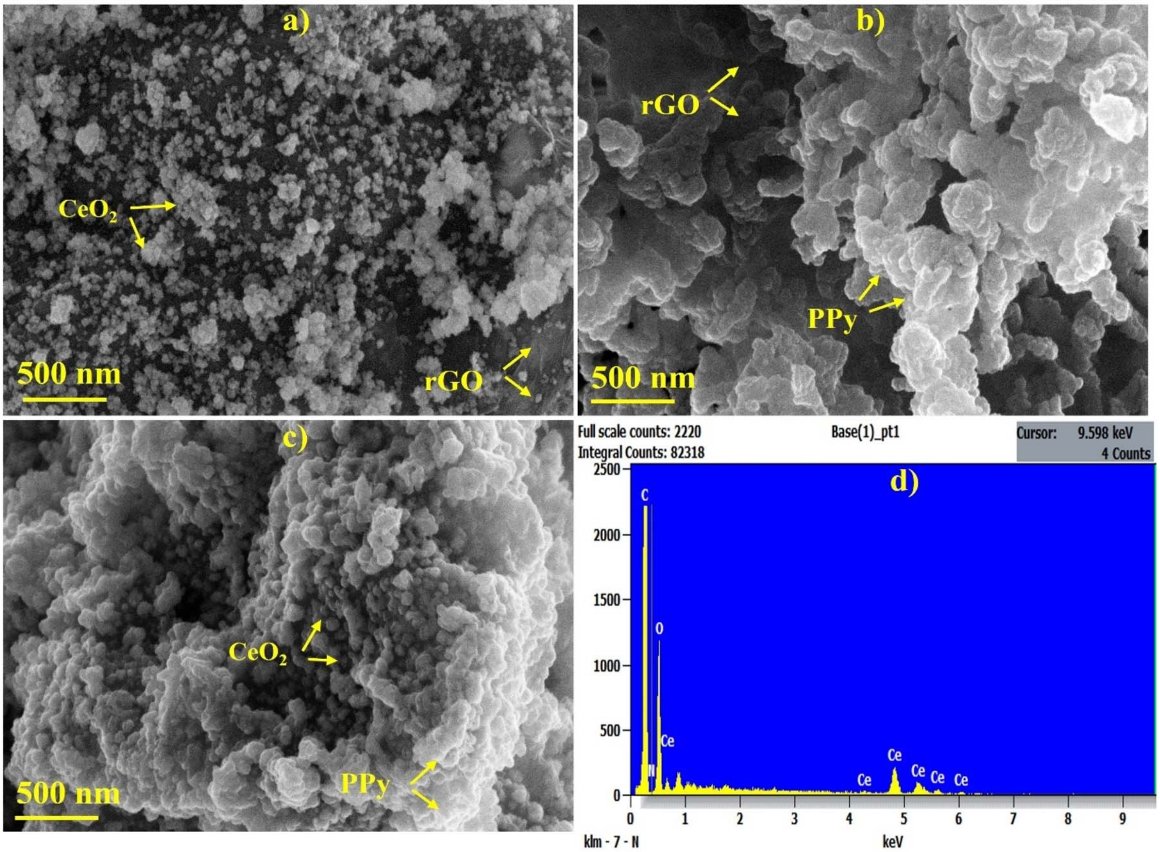

Fig. 7 The SEM images recorded at 500 nm (a) RC, (b) RP, (c) RCP, (d) EDX of RCP.

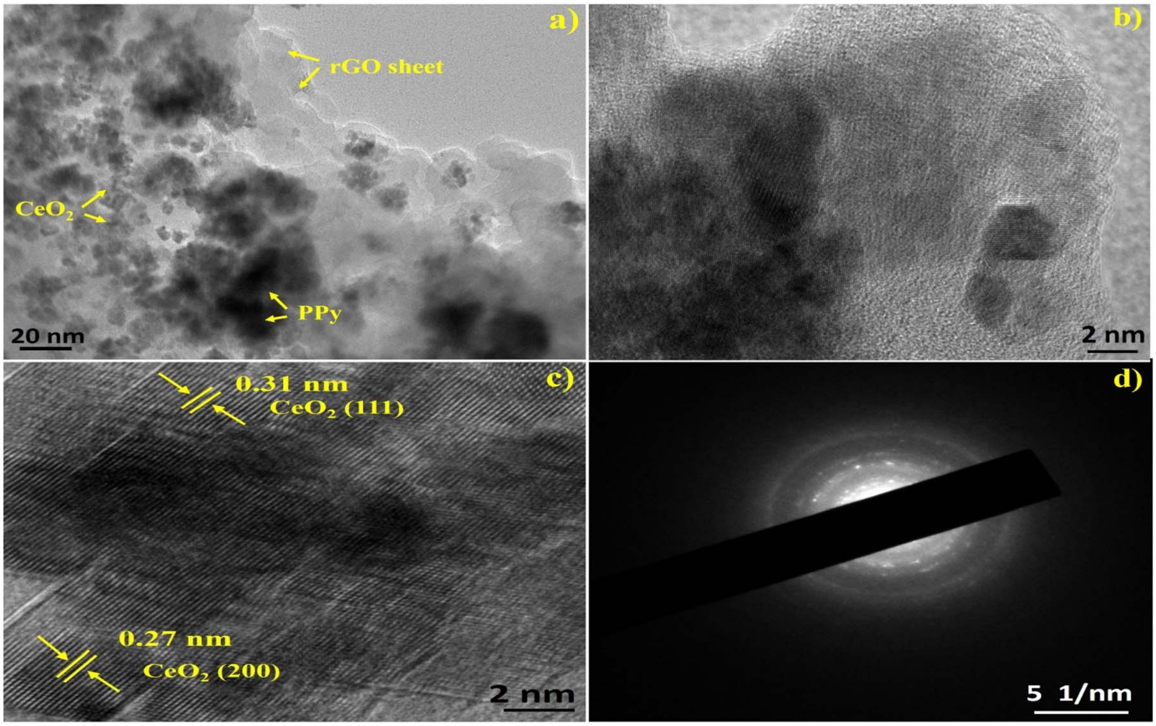

Fig. 8 (a–c) The HRTEM images of RCP recorded at different magnifications, (d) SEAD pattern of RCP.

peaks, indicative of a hybrid charge storage mechanism involving both electric double-layer capacitance (EDLC) and faradaic pseudocapacitance, with the latter being predominant.[60] The ternary RCP composite demonstrated significantly larger CV loop integration compared to pristine GO and binary composites (RC, RP), highlighting its superior charge storage capacity (Fig. 9a). This augmented performance arises from the synergistic interplay between EDLC from the rGO framework and robust pseudocapacitive contributions from CeO$_2$ and PPy. The integration of CeO$_2$ and PPy within the rGO framework effectively suppresses graphene restacking while augmenting electroactive sites and charge transfer kinetics.[61]

The underlying redox mechanism governing the electrochemical behavior can be represented by the following reaction:

$$\mathrm{CeO_2 + M^+ + e^- \leftrightarrow CeOOM}$$

where M$^+$ denotes the alkali cation (K$^+$).[62] During charging, CeO$_2$ is converted into CeOOM, while during discharging, CeOOM reverts to CeO$_2$ through reversible faradaic reactions. The distinct redox peaks observed in the CV profiles further confirm the Faradaic-dominated mechanism, associated with the reversible Ce^{3+}/Ce^{4+} transitions. Specifically, the anodic peak corresponds to the oxidation of Ce^{3+} to Ce^{4+}, whereas the cathodic peak indicates the reduction of Ce^{4+} back to Ce^{3+}.[63,64] The integration of cerium ions into the PPy matrix markedly improves its electrochemical performance by providing extra redox-active sites and refining the structural characteristics of the material. The Ce^{3+}/Ce^{4+} redox couple promotes pseudocapacitance, boosting both charge storage capacity and cycling stability. Additionally, cerium ions encourage the formation of paramagnetic centers, which increase charge carrier density and enhance electrical conductivity. Moreover, PPy synergistically enhances pseudocapacitance and electrical conductivity, optimizing electrochemical performance. Systematic CV analysis, as illustrated in Fig. 9b–d, reveals predictable peak potential separation with escalating scan rates, exhibiting positive anodic and negative cathodic shifts while maintaining well-defined peak morphology.[65] This exceptional retention of electrochemical signature across varied scan rates underscores the composite's outstanding reaction reversibility and minimal polarization effects, confirming its potential for sophisticated energy storage applications.

The correlation between peak current and the square root of the scan rate is typically examined in CV profiles measured at varying scan rates (Fig. 10a). This relationship provides valuable insight into the kinetics of redox reactions at the electrode–electrolyte interface.[66] The assessment of the kinetic mechanism of charge storage involved analyzing CV measurements at different scan rates and applying the power-law rule eqn (4):

$$i = av^b \tag{4}$$

The variables i and v denote the measured current and scan rate, respectively, with a and b being constants. Taking the logarithm of both sides of eqn (5) leads to

$$\log \quad i = \log \quad a + b \quad \log \quad v \tag{5}$$

The b value reflects the rate-limiting process: a value near 0.5 signifies diffusion-controlled electrochemical reactions (typical

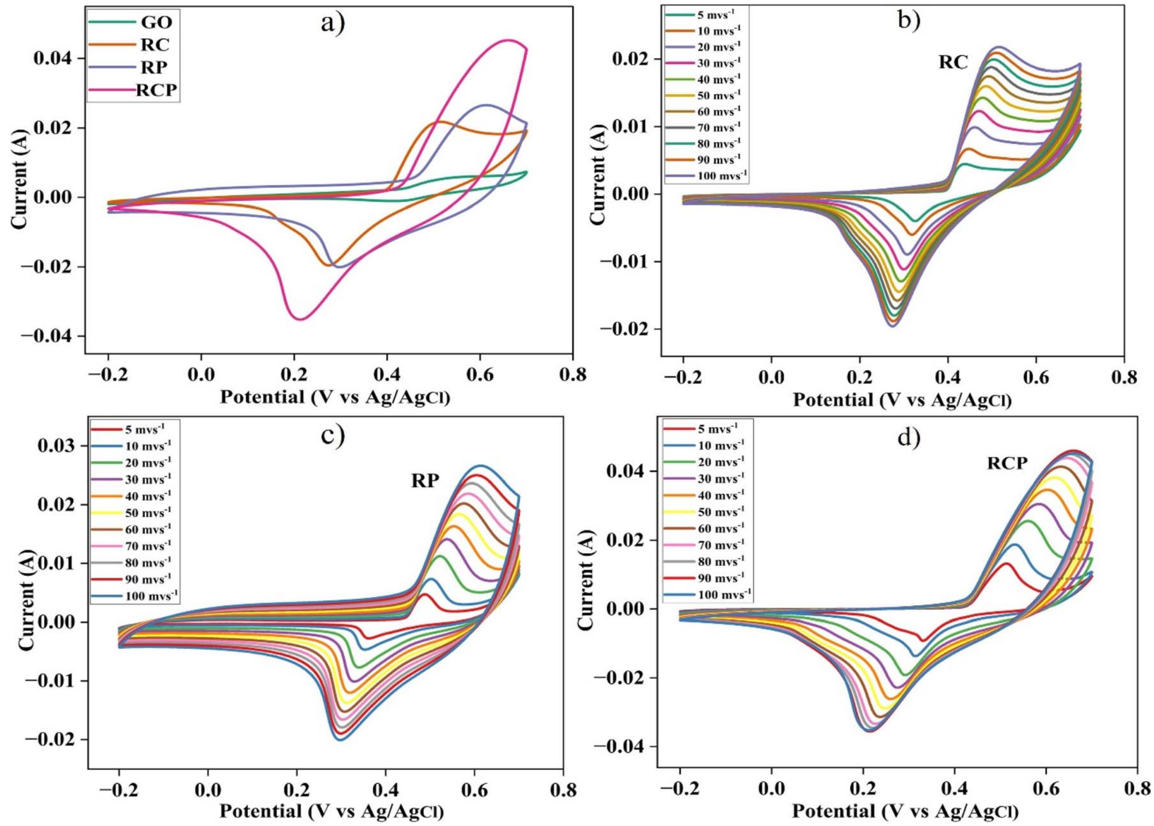

Fig. 9 (a) Cyclic voltammogram comparison recorded at a sweep rate of 100 mV s^{-1}; (b)–(d) CV profiles of RC, RP, and RCP recorded at 5 mV s^{-1} to 100 mV s^{-1}.

of battery materials), whereas a value close to 1 suggests that the reactions are primarily surface-controlled (characteristic of capacitive materials)[67] (Fig. 10b).

The value of '*b*' was determined to be 0.51, indicating a dominant battery-like, diffusion-controlled charge storage mechanism in the RCP nanocomposite.[68] CeO_2 nanoparticles contribute redox-active sites that facilitate reversible redox reactions (Ce^{3+}/Ce^{4+}), while the reduced graphene oxide (rGO) provides a highly conductive network that enhances electron transport, and polypyrrole (PPy) acts as a pseudocapacitive material contributing to additional faradaic processes. This combination of ternary nanocomposite synergistically enhances the charge storage capacity by coupling both faradaic (CeO_2 and PPy) and capacitive effects (rGO), with the diffusion-

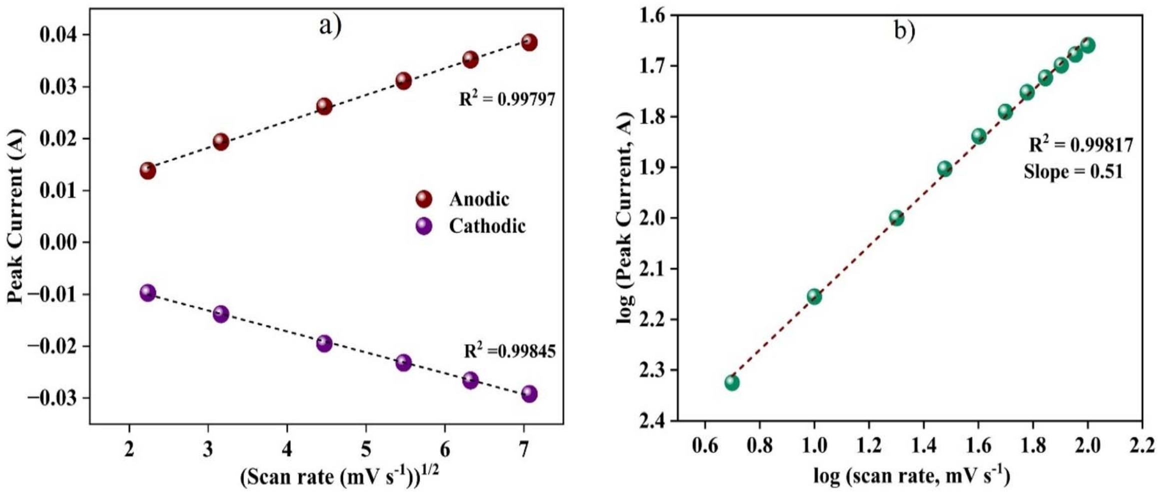

Fig. 10 (a) The plot of anodic and cathodic peak current *vs.* square root of scan rate of RCP; (b) plot of log peak current *vs.* log scan rates.

controlled mechanism playing a major role in overall performance.

The electrochemical performance of GO and its composite electrodes (RC, RP, RCP) was thoroughly evaluated through GCD analysis within a potential range of −0.2 to 0.5 V (*vs.* Ag/AgCl) at 1 A g^{-1} (Fig. 11a). All electrodes exhibited characteristic nonlinear discharge curves with negligible IR drop, indicative of a hybrid charge storage mechanism combining faradaic pseudocapacitance from CeO_2 and PPy redox reactions and electric double-layer capacitance contributed by rGO.[69] The ternary RCP composite demonstrated exceptional electrochemical performance, exhibiting the longest discharge duration, which directly correlates with its superior specific capacitance. This enhanced performance originates from the composite's optimized hierarchical porous architecture that simultaneously maximizes electroactive surface area and facilitates efficient ion diffusion.[70] The rGO framework provides structural stability and enhanced conductivity, while the incorporated CeO_2 nanoparticles prevent graphene restacking and contribute additional redox-active sites. Meanwhile, the uniformly dispersed PPy nanostructures serve dual functions as both conductive bridges and physical spacers, enabling rapid electron transfer and efficient electrolyte penetration in the RCP ternary composite.

All electrodes demonstrate characteristic capacitance attenuation with increasing current density, as illustrated in Fig. 11b–d, reflecting inherent kinetic limitations where elevated rates impede electrolyte penetration and faradaic reaction kinetics.[71] The specific capacitance of the fabricated RC, RP, and RCP electrodes was calculated from the GCD curves using eqn (1) at different current densities, as detailed in Fig. S4 and Table S1.

The specific capacitance value of RCP composite (874 F g^{-1}) outperformed both the binary counterparts RC (402 F g^{-1}), RP (577 F g^{-1}), and pure GO (228 F g^{-1}). The results conclusively establish the ternary composite's potential as a high-efficiency electrode material for next-generation supercapacitor devices, combining optimal nanostructure design with synergistic charge storage mechanisms.

As tabulated in Table 1, a critical comparison of our work with the existing literature data quantitatively establishes the significant performance of our system, achieving superior specific capacitance and long-term durability.

Electrochemical impedance spectroscopy (EIS) experiments were performed to investigate the charge storage dynamics and interfacial reaction kinetics of electrode materials, as showcased in the Nyquist spectral plots (Fig. 12a).[85] All electrodes exhibited characteristic impedance features, including a depressed semicircle arc in the high frequency region, corresponding to charge transfer resistance (R_{ct}) at the electrode–electrolyte interface, followed by a linear Warburg region in the low frequency domain, signifying the ion diffusion process.[86]

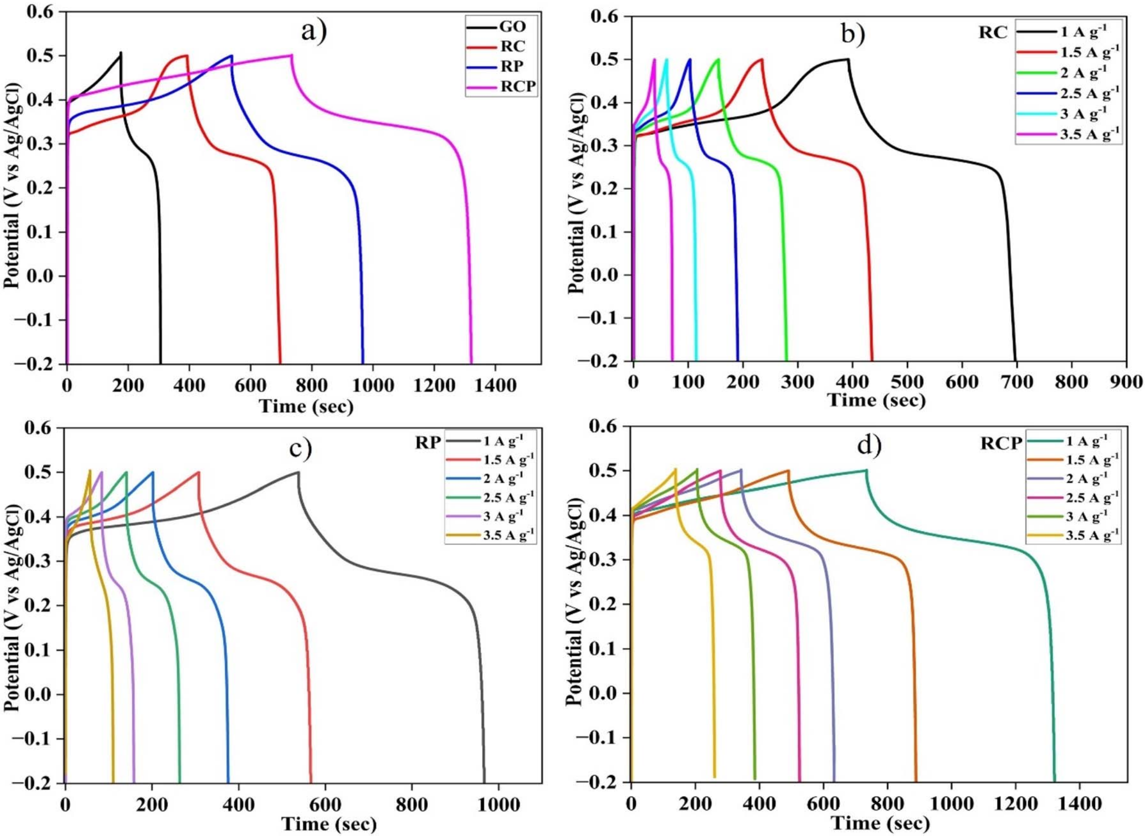

Fig. 11 (a) Comparison of GCD curves recorded at 1 A g^{-1}. (b–d) GCD profiles of RC, RP, and RCP over 1.0 to 3.5 A g^{-1}.

Table 1 A comparative assessment of our work with previously published literature

Composite materials	Synthesis methods	Electrolyte used	Specific capacitance (F g^{-1})	Cycling stability (%)	References
CeO_2	Hydrothermal	3 M KOH	644	90.4	72
CeO_2/CeS_2	Hydrothermal	0.1 M KOH	420	100	73
CeO_2/AC	Hydrothermal	6 M KOH	752	97.5	74
CeO_2/rGO	Self-assembly with annealing	2 M KOH	195	96.2	75
rGO/PPy/PSS	Hydrothermal	0.1 M KOH	313.26	97.6	76
rGO/Co_3O_4/PPy	Hydrothermal with *in situ* polymerization	6 M KOH	532.8	100	77
rGO/CeO_2	Hydrothermal	2 M KOH	616	82	78
CeO_2-doped Zr nanoparticles	Ultrasonic-assisted synthesis	1M KOH	198	94.9	79
Ce-doped Co_3O_4	Solution combustion method	6 M KOH	603.3	87	80
rGO/PPy	*In situ* polymerization	1 M H_2SO_4	675	85	81
CeO_2/Co_3O_4/PEDOT	Hydrothermal with polymerization	3 M KOH	617.8	91.8	82
rGO/PANI/$SrFe_{12}O_{19}$	Sol–gel process with polymerization	1 M H_2SO_4	684	98.96	83
rGO/PPy	SILAR method	1 M H_2SO_4	803	91	84
rGO/CeO_2/PPy	Hydrothermal followed by *in situ* polymerization	2 M KOH	874	94	(This work)

The RCP composite demonstrated superior electrochemical properties, evidenced by its near-vertical Warburg slope, which reflects optimized ion diffusion kinetics facilitated by its hierarchical porous architecture. Notably, the ternary composite exhibited significantly reduced R_{ct} and solution resistance R_s values compared to other samples, attributed to the synergistic combination of highly conductive rGO networks, redox-active CeO_2 nanoparticles, and electrochemically responsive PPy matrices. These results collectively highlight the RCP composite's exceptional charge transfer characteristics and minimal interfacial resistance, demonstrating its potential as an advanced electrode material for high-performance energy systems.

The cycling stability serves as a critical benchmark for evaluating the long-term electrochemical viability and structural integrity of the electrode materials. As evidenced in (Fig. 12b), the ternary RCP composite exhibited remarkable capacitance retention (94%) across 5000 charge/discharge cycles at 3 A g^{-1}, emphasizing its superior mechanical endurance and electrochemical reliability. This enhanced stability arises from the incorporation of rGO as a conductive and mechanically robust framework, which effectively buffers structural stress induced by the repeated redox reactions of CeO_2 and PPy. To confirm the morphological integrity, and electrochemical stability of the RCP electrode, SEM, XRD and EIS analysis were conducted after 5000 cycles as showcased in Fig. S5 and S6. The electrode maintains its structural framework without ant structural degradation, demonstrating excellent mechanical and morphological stability as illustrated in Fig. S5. Moreover, electrochemical impedance spectroscopy (EIS) measurements were done before and after 5000 cycles (Fig. S6) The Nyquist plots shows that the charge-transfer resistance exhibits only a negligible increase after cycling, confirming that the internal resistance remains stable during long-term operation. This observation further supports the outstanding cycling performance and stability.

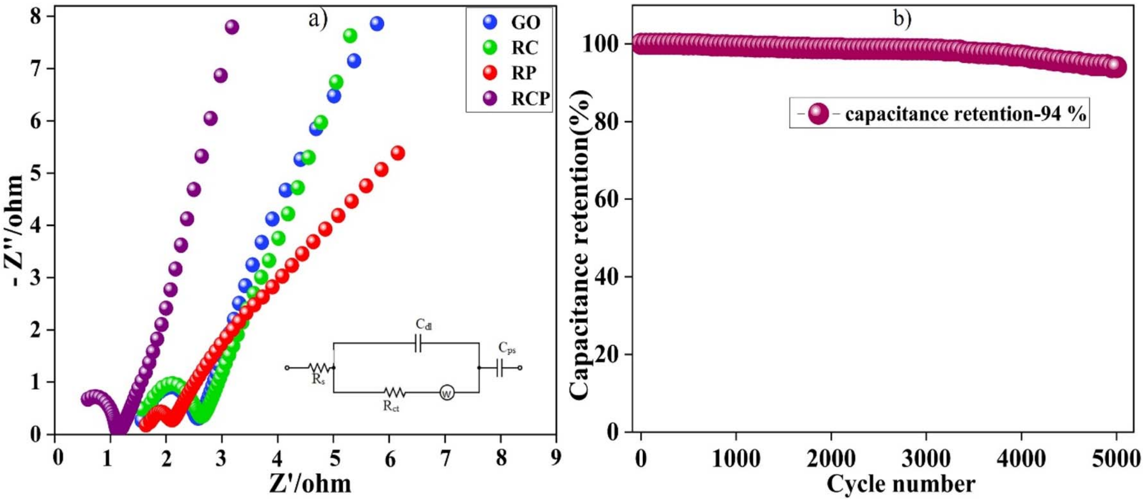

Fig. 12 (a) The EIS spectra obtained for GO, RC, RP, and RCP; (b) the cycling stability test of RMC composite.

3.4 Fabrication of rGO/CeO$_2$/PPy//AC asymmetric supercapacitor

The performance matrices of the fabricated rGO/CeO$_2$/PPy//AC asymmetric supercapacitor were examined using various analytical techniques. The cyclic voltammetry analysis conducted for the rGO/CeO$_2$/PPy//AC device (10–100 mV s^{-1}) revealed a unique CV profile, demonstrating exceptional charge compatibility between the faradaic and non-faradaic components (Fig. 13a). The cathodic process demonstrated battery-type behavior through reversible intercalation/de-intercalation reactions, while the anode exhibited electric double-layer capacitive characteristics *via* ionic adsorption/desorption. Remarkable electrochemical stability was evidenced by well-maintained CV profiles across increasing scan rates, indicating superior reversibility and rate performance of the device.

The charge storage performance of the asymmetric supercapacitor was further corroborated through galvanostatic charge–discharge analysis across an extended potential range of 0.0–1.4 V (Fig. 13b). The GCD curves obtained were symmetric but non-linear in nature, albeit with slight distortion, which validates the combined pseudocapacitive and EDLC-based charge storage mechanism. As evidenced by the calculated gravimetric capacitances, the device delivered outstanding specific capacitances of 145.7, 132.8, 120, 107, and 94 F g^{-1} at progressively increasing current densities of 1.0, 1.5, 2.0, 2.5, and 3.0 A g^{-1}, respectively (Fig. 13c). These results underscore the device's remarkable rate capability, as it maintains a substantial fraction of its initial capacitance even under elevated current densities, reflecting efficient charge storage kinetics and robust electrochemical stability. The Nyquist plot obtained for the asymmetric supercapacitor (Fig. 13d) showcases a very low charge transfer resistance, which exemplifies the device's advanced capacitive properties, highlighting efficient pathways for swift electron and ion transport, which is crucial for high-performance energy storage devices.

The energy and power densities of the hybrid supercapacitor were assessed through galvanostatic charge–discharge (GCD) analysis, employing eqn (2) and (3) (Fig. 14a). Notably, the system showcased an exceptional energy density of 39.67 Wh kg^{-1} at a power density of 2859 W kg^{-1}, surpassing the performance of many previously reported systems. Remarkably, even at an elevated power density of 6535 W kg^{-1}, the device retained an energy density of 19.9 Wh kg^{-1}, highlighting its ultrafast energy storage capability. Remarkably, even at an elevated power density of 6535 W kg^{-1}, the device retained an energy density of 19.9 Wh kg^{-1}, highlighting its ultrafast energy storage capability. The comparison of the Ragone plot with other related systems is showcased in Fig. 14b.

A comparative assessment of the Ragone plot of the rGO/CeO$_2$/PPy//AC system with previously published literature is given in Table 2.

As illustrated in Fig. 14b, the rGO/CeO$_2$/PPy//AC asymmetric supercapacitor exhibited exceptional electrochemical stability, maintaining highly symmetrical and well-defined charge–

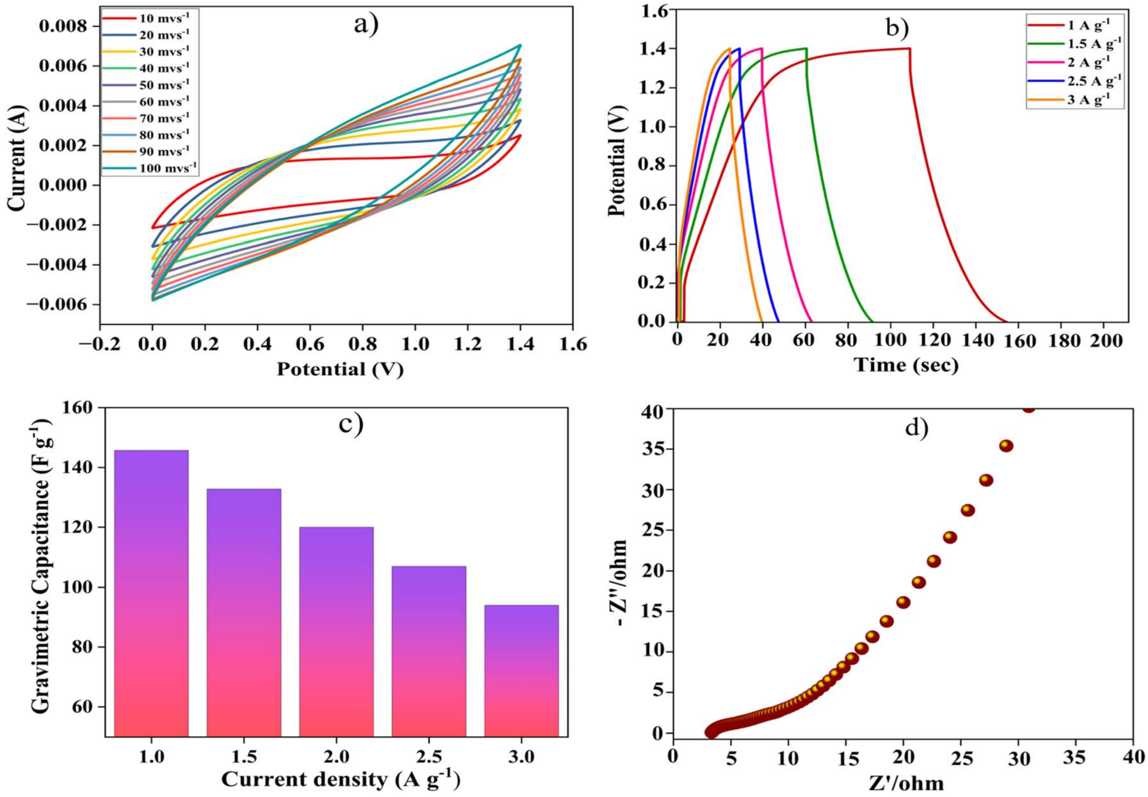

Fig. 13 (a) Cyclic voltammetry studies, (b) charge–discharge profile, (c) variation of gravimetric capacitance with current densities, (d) EIS spectrum obtained for the fabricated device.

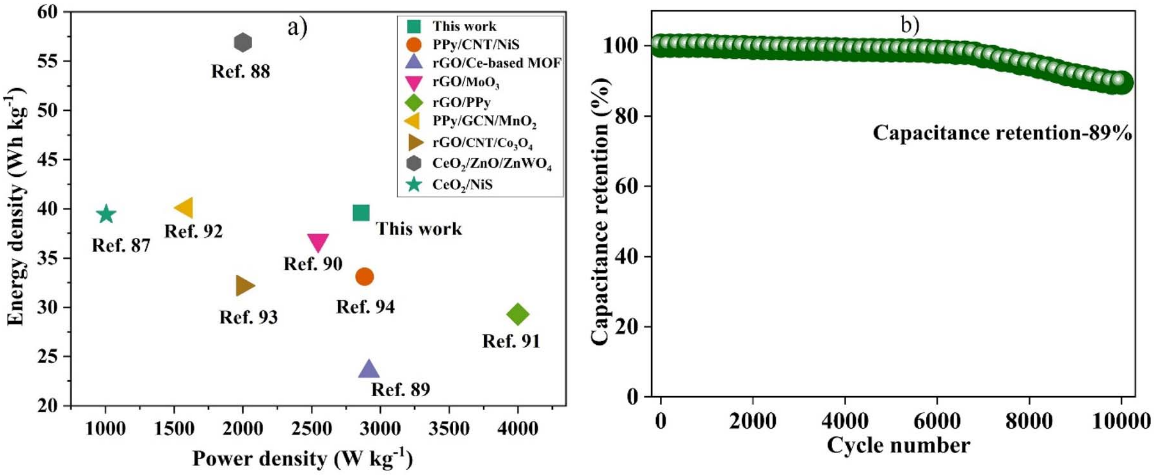

Fig. 14 (a) The comparison of Ragone plot (b) cycling stability test of the fabricated rGO/CeO$_2$/PPy//AC supercapacitors.

Table 2 A comparative assessment of the Ragone plot of the rGO/CeO$_2$/PPy//AC system with previously published literature

Reported systems	Energy density (Wh kg^{-1})	Power density (W kg^{-1})	References
CeO$_2$/NiS	39.4	1006	87
CeO$_2$/ZnO/ZnWO$_4$	56.9	2000	88
rGO/CNT/Co$_3$O$_4$	32.2	2000	89
PPy/GCN/MnO$_2$	40.1	1587.6	90
rGO/PPy	29.3	4000	91
rGO/MoO$_3$	36.78	2546.8	92
rGO/Ce-based MOF	23.5	2917.12	93
PPy/CNT/NiS	33.12	2885	94
This work	39.67	2859	—

discharge profiles even after extensive cycling. Remarkably, the fabricated device showed 89% capacitance retention, underscoring its outstanding long-term cyclability and operational durability under sustained electrochemical stress.

4. Conclusion

Two-dimensional reduced graphene oxide, when combined with pseudocapacitive materials, holds significant potential for fabricating advanced supercapacitors. This research reports the synthesis of a ternary composite, rGO/CeO$_2$/PPy, through a combination of hydrothermal synthesis and *in situ* polymerization. The composite electrode exhibits a distinctive porous structure and remarkable electrochemical properties, achieving a high C_{sp} of 874 F g^{-1} at a current density of 1 A g^{-1}. Impressively, the electrode retains 94% of its initial capacitance after 5000 charge–discharge cycles, demonstrating exceptional cycling stability. The sheet-like structure of rGO provides a stable substrate for the uniform growth of CeO$_2$ nanoparticles and effectively mitigates their aggregation. The *in situ* polymerized PPy significantly improves electrical conductivity, thereby augmenting the overall electrochemical activity. The robust three-dimensional porous structure of the composite facilitates enhanced ion transport and charge storage capabilities. Moreover, the synergistic interactions and strong π–π conjugation among the components contribute to the composite's superior energy storage characteristics. The fabricated rGO/CeO$_2$/PPy//AC device showcased a remarkable energy and power density of 39.67 Wh kg^{-1} and 2859 W kg^{-1}, respectively, underscoring the exceptional performance derived from the combination of pseudocapacitance and electric double-layer capacitance (EDLC) contributions. The supercapacitor retained 89% of its capacitance at 5 A g^{-1} after 5000 cycles. The demonstrated performance metrics of these hybrid materials establish a new paradigm for designing high-performance supercapacitive systems for efficient energy storage solutions.

Author contributions

Nirosha James: writing – original draft, conceptualization, visualization, methodology, validation, investigation, formal analysis, data curation. Amala Shaliya Joseph: formal analysis, validation, resources. Abhirami Krishna: validation, data curation. Sreeja P. B: writing – review & editing, conceptualization, supervision, validation, funding acquisition, data curation.

Conflicts of interest

The authors declare that there are no financial, professional, or personal conflicts of interest that could have influenced the findings or conclusions of this study.

Data availability

The authors declare that the data collected during analysis are documented in the relevant sections of this article, with additional supporting data provided separately.

Supplementary information is available. See DOI: **https://doi.org/10.1039/d5ra05408g**.

Acknowledgements

The authors gratefully acknowledge the support provided by the Department of Chemistry and the Centre for Renewable Energy and Environmental Sustainability, CHRIST University, Bengaluru.

References

1 M. Srivastava, *et al.*, Exploring the Potential and Roadblocks of Marketable Energy-Storage Technologies for Renewable Energy, *Energy Technol.*, 2025, **13**(8), 2402405, DOI: **10.1002/ente.202402405**.

2 Y. H. Reddy, M. R. Ambika, H. K. Naik, B. M. Basavaraja and N. Nagaiah, An overview on MXene/rare earth and transition metal oxide hybrid composites for supercapacitor applications, *Ionics*, 2025, **31**, 5325–5349, DOI: **10.1007/s11581-025-06248-7**.

3 I. Hussain, *et al.*, Practicality of MXenes: recent trends, considerations, and future aspects in supercapacitors, *Mater. Today Phys.*, 2025, **55**, 101745, DOI: **10.1016/j.mtphys.2025.101745**.

4 D. H. Adebayo, J. A. Ajiboye, U. D. Okwor and A. L. Muhammad, Optimizing energy storage for electric grids : advances in hybrid technologies, *World Journal of Advanced Engineering Technology and Sciences*, 2025, **14**(02), 138–172, DOI: **10.30574/wjaets.2025.14.2.0053**.

5 L. Wang, N. Tricard and Z. Chen, Progress in computational methods and mechanistic insights on the growth of carbon nanotubes, *Nanoscale*, 2025, **17**, 11812–11863, DOI: **10.1039/d4nr05487c**.

6 S. Banerjee, B. Mordina, P. Sinha and K. K. Kar, Recent advancement of supercapacitors: a current era of supercapacitor devices through the development of electrical double layer, pseudo and their hybrid supercapacitor electrodes, *J. Energy Storage*, 2025, **108**, 115075, DOI: **10.1016/j.est.2024.115075**.

7 A. Pramanik, *et al.*, Ternary Metal Sulfides as Electrode Materials for Na/K-Ion Batteries and Electrochemical Supercapacitor: Advances/Challenges and Prospects, *Adv. Energy Mater.*, 2024, **14**(36), 2401657, DOI: **10.1002/aenm.202401657**.

8 L. Liu, X. Zhang, Y. Liu and X. Gong, Electrochemical Energy Storage Devices─Batteries, Supercapacitors, and Battery–Supercapacitor Hybrid Devices, *ACS Appl. Electron. Mater.*, 2025, 7, 2233–2270, DOI: **10.1021/acsaelm.5c00069**.

9 Y. Wang, *et al.*, Carbonaceous materials in structural dimensions for advanced oxidation processes, *Chem. Soc. Rev.*, 2025, 2436–2482, DOI: **10.1039/d4cs00338a**.

10 D. Bhatt, T. Kokulnathan, T.-J. Wang, M. A. Ghanem and N. G. Sahoo, Powering sustainability: high-performance supercapacitors using reduced graphene oxide from waste tires embedded with molybdenum disulfide, *J. Power Sources*, 2025, **642**, 236932, DOI: **10.1016/j.jpowsour.2025.236932**.

11 L. Liu, *et al.*, Graphene-based polymer composites in thermal management: materials, structures and applications, *Mater. Horizons*, 2024, **12**(1), 64–91, DOI: **10.1039/d4mh00846d**.

12 A. Kashyap, B. Dehingia, R. Ghosh and H. Kalita, Recent Progress on Graphene-Based Derivatives for Enhanced Energy Storage Devices, *Chem.–An Asian J.*, 2025, **20**(11), e202401794, DOI: **10.1002/asia.202401794**.

13 N. Bisht, *et al.*, Synergizing chemistry: unveiling the potential of hybrid fillers for enhanced performance in shape memory polymers, *Adv. Compos. Hybrid Mater.*, 2025, **8**(7), 10–12, DOI: **10.1007/s42114-024-01059-2**.

14 V. Vijayakanth, *et al.*, Synergistic effects in Co-doped $NiFe_2O_4$/rGO/MWCNT ternary nanocomposites for enhanced supercapacitor performance, *Diam. Relat. Mater.*, 2025, **158**, 112679, DOI: **10.1016/j.diamond.2025.112679**.

15 S. H. Bangash, *et al.*, Ni-incorporated $Co(OH)_2$ nanowires on nickel foam as an advanced electrode material for supercapacitor, *Microchem. J.*, 2025, **215**, 114208, DOI: **10.1016/j.microc.2025.114208**.

16 D. Deng, *et al.*, Cerium oxide nanoparticles/multi-wall carbon nanotubes composites: facile synthesis and electrochemical performances as supercapacitor electrode materials, *Phys. E*, 2017, **86**, 284–291, DOI: **10.1016/j.physe.2016.10.031**.

17 B. Jeong, *et al.*, Artificial Synaptic Properties in Oxygen-Based Electrochemical Random-Access Memory with CeO_2 Nanoparticle Assembly as Gate Insulator for Neuromorphic Computing, *ACS Appl. Mater. Interfaces*, 2025, **17**(11), 17105–17116, DOI: **10.1021/acsami.5c00027**.

18 J. Cao, *et al.*, 3D-Printed porous MnO_2/Carbon composites synthesized *via* fast joule heating for energy storage electrodes, *Chem. Eng. J.*, 2025, **505**, 159723, DOI: **10.1016/j.cej.2025.159723**.

19 T. Liu, *et al.*, Two-dimensional nanostructures of transition metal-based materials towards aqueous electrochemical energy storage, *Chem. Commun.*, 2025, 5094–5109, DOI: **10.1039/d4cc06341d**.

20 I. O. Oladele, *et al.*, Polymer-based nanocomposites for supercapacitor applications: a review on principles, production and products, *RSC Adv.*, 2025, **15**, 7509–7534, DOI: **10.1039/D4RA08601E**.

21 T. Divya, R. Sarankumar, K. S. Balamurugan, P. Sakthivel and A. Sivakami, Recent advances in transition metal oxide composites for enhanced supercapacitor performance: a comprehensive overview, *J. Nanoparticle Res.*, 2025, **27**, 1–21, DOI: **10.1007/s11051-025-06246-w**.

22 V. Jayaweera and W. L. N. C. Liyanage, Material Science Research India Composite for High-Performance Supercapacitors, *Mater. Sci. Res. India*, 2021, **18**, 206–216.

23 M. Ates, C. Alperen, Y. Bayrak and O. Yoruk, Pore size, conductivity and surface area effects of rGO/ZnO/PTh hybrid nanocomposite for supercapacitors, *Diam. Relat. Mater.*, 2024, **147**, 111230, DOI: **10.1016/j.diamond.2024.111230**.

24 V. Gadore, S. R. Mishra and M. Ahmaruzzaman, One-pot synthesis of CdS/CeO_2 heterojunction nanocomposite with tunable bandgap for the enhanced advanced oxidation

process, *Sci. Rep.*, 2023, **13**, 1–18, DOI: **10.1038/s41598-023-34742-3**.

25 N. James, S. Simon, S. Rajeevan, S. C. George and S. P. Balakrishnan, Symmetric Supercapacitors based on Reduced Graphene Oxide/Multi-walled Carbon Nanotubes/Cobalt Oxide Ternary Composites, *J. Macromol. Sci. Part B Phys.*, 2023, 1–22, DOI: **10.1080/00222348.2023.2285656**.

26 H. Vijeth, *et al.*, Influence of nickel oxide nanoparticle on the structural, electrical and dielectric properties of polypyrrole nanocomposite, *AIP Conf. Proc.*, 2019, **2142**, 1–6.

27 L. Liu, M. Du and F. Liu, Recent advances in interface microscopic characterization of carbon fiber-reinforced polymer composites, *Front. Mater.*, 2023, **10**, 1–18, DOI: **10.3389/fmats.2023.1124338**.

28 S. K. Samdarshi, *et al.*, Oxygen vacancies induce changes in lattice parameter, photoluminescence characteristics and Raman spectra of sol–gel derived fluorite-type cubic CeO_2 and $Ce_{0.8}Zr_{0.2} - xA_xO_2$ (A = Co/Fe, $x = 0 - 0.2$) powders, *Appl. Phys. A*, 2022, **128**, 712, DOI: **10.1007/s00339-022-05860-y**.

29 J. Ma, dans une pile microfluidique Pour l ' obtention du Grade de (Faculté des Sciences Fondamentales et Appliquées) Ecole Doctorale μ Sciences pour l ' Environnement Gay δussac Secteur de Recherche : Chimie Théorique , Physique, *Analytique Présentée Par : D*, 2013.

30 F. Inoue, R. A. Ando, C. M. S. Izumi and P. Corio, Spectroscopic Characterization of Carbon Nanotube-Polypyrrole Composites, *J. Phys. Chem. C*, 2014, **118**(31), 18240–18248, DOI: **10.1021/jp505525k**.

31 T. Runka, Spectroscopic properties of polymer composites, *Phys. Sci. Rev.*, 2017, **2**(8), 20170025, DOI: **10.1515/psr-2017-0025**.

32 N. Chakrabarty, S. Krishnamurthy, *et al.*, CeO_2/Ce_2O_3 quantum dot decorated reduced graphene oxide nanohybrid as electrode for supercapacitor, *Appl. Surf. Sci.*, 2021, **536**, 147960, DOI: **10.1016/j.apsusc.2020.147960**.

33 M. Dhanda, R. Arora, A. Sudharshan Reddy, *et al.*, Coalescing of lanthanum oxide and PPy @graphitic carbon nitride to achieve ultrahigh energy density electrode material for supercapacitor applications, *J. Alloys Compd.*, 2023, **955**, 169738, DOI: **10.1016/j.jallcom.2023.169738**.

34 B. Soni, S. Makkar and S. Biswas, Defects induced tailored optical and magnetic properties of Zn-doped CeO_2 nanoparticles synthesized by a facile sol-gel type process, *J. Alloys Compd.*, 2021, **879**, 160149, DOI: **10.1016/j.jallcom.2021.160149**.

35 K. Chakarova, M. Mihaylov and K. Hadjiivanov, Can two CO_2 molecules be simultaneously bound to one Na^+ site in NaY zeolite? a detailed FTIR investigation, *Microporous Mesoporous Mater.*, 2022, **345**, 112270, DOI: **10.1016/j.micromeso.2022.112270**.

36 S. Azeez and R. Shenbagaraman, 8 – Fourier transform infrared spectroscopy in characterization of bionanocomposites, *Characterization Techniques in Bionanocomposites: Advances, Challenges, and Applications*, Woodhead Publishing Series in Composites Science and Engineering, Woodhead Publishing, 2025, pp. 209–227, DOI: **10.1016/B978-0-443-22067-8.00008-3**.

37 O. C. Altıncı and B. K. Körbahti, Graphene oxide-polyaniline conducting composite film deposited on platinum-iridium electrode by electrochemical polymerization of aniline: Synthesis and environmental electrochemistry application, *Appl. Surf. Sci. Adv.*, 2022, **7**, 100212, DOI: **10.1016/j.apsadv.2022.100212**.

38 M. Boopathi, P. Udhayakala, T. V. Rajendiran and S. Gunasekaran, Theoretical Calculation of Molecular Structure, Vibrational Spectra, and Molecular Electrostatic Potential of Metolazone, *J. Appl. Spectrosc.*, 2016, **83**, 12–19, DOI: **10.1007/s10812-016-0235-z**.

39 G. M. do Nascimento and M. A. de Souza, Spectroscopy of Nanostructured Conducting Polymers, *Nanostructured Conductive Polymers*, 2010, DOI: **10.1002/9780470661338.ch8**.

40 K. Morishige, Pore Size Distribution Analysis Using Developing Hysteresis of Nitrogen in the Cylindrical Pores of Silica, *Langmuir*, 2022, **38**, 4222–4233, DOI: **10.1021/acs.langmuir.1c03219**.

41 N. James, S. Mathew, J. Mary and P. B. Sreeja, *J. Energy Storage*, 2025, **134**, 118287, DOI: **10.1016/j.est.2025.118287**.

42 N. James and S. PB, Indium oxide decorated graphitic carbon nitride/multiwalled carbon nanotubes ternary composite for supercapacitor applications, *Electrochim. Acta*, 2024, **507**, 145192, DOI: **10.1016/j.electacta.2024.145192**.

43 N. James, S. Simon and P. B. Sreeja, Materials Today : Proceedings Electrochemical performance of rGO/MWCNT/CoS ternary composite for supercapacitor applications, *Mater. Today Proc.*, 2023, DOI: **10.1016/j.matpr.2023.11.076**.

44 M. A. Isaacs, *et al.*, Advanced XPS characterization: XPS-based multi-technique analyses for comprehensive understanding of functional materials, *Mater. Chem. Front.*, 2021, **5**, 7931–7963, DOI: **10.1039/D1QM00969A**.

45 Q. Tong, S. Liu, J. Liang, Q. Zhang and M. Liao, Structure and quantification of Ce^{3+}/Ce^{4+} and stability analysis of basaltic glasses for the immobilization of simulated tetravalent amines, *Sci. Rep.*, 2025, **15**, 2288, DOI: **10.1038/s41598-025-86571-1**.

46 Z. Li, *et al.*, Enhanced photocatalytic performance by regulating the Ce^{3+}/Ce^{4+} ratio in cerium dioxide, *Front. Chem. Sci. Eng.*, 2024, **18**, 31, DOI: **10.1007/s11705-024-2394-4**.

47 S. K. Ray, *et al.*, Recent Progress on Cerium Oxide-Based Nanostructures for Energy and Environmental Applications, *Adv. Energy Sustain. Res.*, 2025, 2500022, DOI: **10.1002/aesr.202500022**.

48 M. Dave, *et al.*, Ferromagnetic interactions and luminescence in Dy-doped CeO_2 nanoparticles with regard of defects and electronic structure, *J. Mater. Sci. Mater. Electron.*, 2025, **36**, 572, DOI: **10.1007/s10854-025-14594-5**.

49 X. Chen, X. Wang and D. Fang, A review on C1s XPS-spectra for some kinds of carbon materials, *Fullerenes Nanotub. Carbon Nanostructures*, 2020, 1048–1058, DOI: **10.1080/1536383X.2020.1794851**.

50 M. Kehrer, *et al.*, XPS investigation on the reactivity of surface imine groups with TFAA, *Plasma Process. Polym.*, 2019, **16**(4), 1800160, DOI: **10.1002/ppap.201800160**.

51 Y. Gao, *et al.*, Self-Assembled Composite Cathodes with TEC Gradient for Proton-Conducting Solid Oxide Fuel Cells, *Adv. Funct. Mater.*, 2024, 2416625, DOI: **10.1002/adfm.202416625**.

52 S. Simon, N. James, S. Rajeevan, S. C. George and P. B. Sreeja, Sandwich structured pedot-TiO_2/GO/PEDOT-TiO_2 electrodes for supercapacitor, *Results Chem.*, 2023, **6**, 101144, DOI: **10.1016/j.rechem.2023.101144**.

53 Y. Du, *et al.*, Flexible graphene-based composite films for energy storage devices: From interfacial modification to interlayer structure design, *Chem. Eng. J.*, 2024, **493**, 152704, DOI: **10.1016/j.cej.2024.152704**.

54 N. James, S. Simon and P. B. Sreeja, Graphene–Metal Oxide Composite Materials for Supercapacitor Applications, in *Graphene–Metal Oxide Composites: Synthesis, Properties, and Applications*, Moharana, S., Satpathy, S. K. and Nguyen, T. A. and Maharana, T., Royal Society of Chemistry, 2025, DOI: **10.1039/9781837673391-00734**.

55 G. M. Tomboc, *et al.*, Stabilization, Characterization, and Electrochemical Applications of High-Entropy Oxides: Critical Assessment of Crystal Phase–Properties Relationship, *Adv. Funct. Mater.*, 2022, **32**(43), 2205142, DOI: **10.1002/adfm.202205142**.

56 J. Liu, *et al.*, Interfacial component coupling effects towards precise heterostructure design for efficient electrocatalytic water splitting, *Nano Energy*, 2022, **103**, 107753, DOI: **10.1016/j.nanoen.2022.107753**.

57 G. C. Sujay Shekar, K. Alkanad, *et al.*, Surface defect-engineered $CeO_2 - x$ by ultrasound treatment for superior photocatalytic H2 production and water treatment, *Catal. Sci. Technol.*, 2022, **12**, 2071–2083, DOI: **10.1039/D1CY01940F**.

58 M. Vinitha, G. Velraj, K. Anandan, G. K. Meenatchi and M. Shellaiah, Synthesis of PPy/CeO_2 nanocomposites for supercapacitor application, *Int. J. Polym. Anal. Charact.*, 2025, **30**, 122–132, DOI: **10.1080/1023666X.2024.2440504**.

59 Y. Li, J. Zhang, Q. Chen, X. Xia and M. Chen, Emerging of Heterostructure Materials in Energy Storage: A Review, *Adv. Mater.*, 2021, **33**, 2100855, DOI: **10.1002/adma.202100855**.

60 F. Bibi, O. Gerard, A. J. Khan, M. Khalid and A. Numan, in *3 – Categories of pseudocapacitor: intrinsic, extrinsic, and intercalation materials*, ed. Krishnan, S. G., Pham, H. D. and Dubal, D. P. B. T.-S., Elsevier, 2024, pp. 45–70, DOI: **10.1016/B978-0-443-15478-2.00005-X**.

61 W. Zhou, *et al.*, Interfacial oxygen vacancies and energy-level engineering on CeO_2-PPy-rGO nanocomposites towards boosted NO_2 sensor performance, *Sens. Actuators, B*, 2023, **396**, 134614, DOI: **10.1016/j.snb.2023.134614**.

62 G. Veeresha, G. Krishnamurthy and M. S. Shivakumar, Cobalt nanocrystals doped on CeO_2/rGO nanocomposite for supercapacitor applications, *Inorg. Chem. Commun.*, 2022, **138**, 109232, DOI: **10.1016/j.inoche.2022.109232**.

63 S. Kim and Y. J. Sa, Ce^{4+}/Ce^{3+} Redox-Promoted Electron Transfer for Efficient Neutral H_2O_2 Electrosynthesis from Two-Electron Oxygen Reduction, *ACS Catal.*, 2024, **14**, 6842–6855, DOI: **10.1021/acscatal.4c00625**.

64 J. Wu, *et al.*, Boosting Kinetics of Ce^{3+}/Ce^{4+} Redox Reaction by Constructing TiC/TiO^2 Heterojunction for Cerium-Based Flow Batteries, *Adv. Funct. Mater.*, 2024, **34**, 2309825, DOI: **10.1002/adfm.202309825**.

65 A. Salimi and S. Sanjabi, Binder-free copper manganese sulfide nanoflake arrays electrodeposited on reduced graphene oxide-wrapped nickel foam as an efficient battery-type electrode for asymmetric supercapacitors, *J. Power Sources*, 2024, **620**, 235253, DOI: **10.1016/j.jpowsour.2024.235253**.

66 W. U. Arifeen, *et al.*, Binder-free nickel oxalate: a promising material for High-performance electrochemical energy storage in supercapacitors, *J. Electroanal. Chem.*, 2025, **978**, 118882, DOI: **10.1016/j.jelechem.2024.118882**.

67 Sajida, I. Shaheen, I. Hussain, *et al.*, Fabrication of binder-free Ni-Mn oxalate electrode for supercapacitor application, *Electrochim. Acta*, 2025, **513**(10), 145527, DOI: **10.1016/j.electacta.2024.145527**.

68 X. Leng, *et al.*, Hollow-sphere manganese-modified nickel MOF electrodes: redefining energy storage potential for supercapacitor efficiency and durability, *J. Energy Storage*, 2025, **121**, 116572, DOI: **10.1016/j.est.2025.116572**.

69 T. Schoetz, *et al.*, Disentangling faradaic, pseudocapacitive, and capacitive charge storage: a tutorial for the characterization of batteries, supercapacitors, and hybrid systems, *Electrochim. Acta*, 2022, **412**, 140072, DOI: **10.1016/j.electacta.2022.140072**.

70 M. A. Saghafizadeh, A. Mohammadi Zardkhoshoui and S. S. Hosseiny Davarani, Reinforced supercapacitor electrode *via* reduced graphene oxide encapsulated $NiTe_2$–$FeTe_2$ hollow nanorods, *Nanoscale Horiz.*, 2025, **10**, 1159–1172, DOI: **10.1039/D5NH00107B**.

71 Y. Hao, *et al.*, Heterogeneous nanocomposite of MOF-derived (NiCo)Se_2 nanospheres decorated with rare earth oxide nanorods for high-performance electrochemical energy storage, *J. Energy Storage*, 2024, **91**, 112168, DOI: **10.1016/j.est.2024.112168**.

72 N. Padmanathan and S. Selladurai, Shape-controlled synthesis of CeO_2 nanostructures for high-performance supercapacitor electrodes, *RSC Adv.*, 2014, **4**, 6527–6534, DOI: **10.1039/C3RA43339K**.

73 N. Bibi, *et al.*, Highly stable mesoporous CeO_2/CeS_2 nanocomposite as electrode material with improved supercapacitor electrochemical performance, *Ceram. Int.*, 2018, **44**, 22262–22270, DOI: **10.1016/j.ceramint.2018.08.348**.

74 Z. Yang, M. Xiang, W. Zhu, J. Hui and H. Qin, Biomass Heteroatom Carbon/Cerium Dioxide Composite Nanomaterials Electrode for High-Performance Supercapacitors, *ACS Sustain. Chem. Eng.*, 2020, **8**(17), 6675–6681, DOI: **10.1021/acssuschemeng.0c00188**.

75 Z. Ji, X. Shen, H. Zhou and K. Chen, Facile synthesis of reduced graphene oxide/CeO_2 nanocomposites and their application in supercapacitors, *Ceram. Int.*, 2015, **41**(7), 8710–8716, DOI: **10.1016/j.ceramint.2015.03.089**.

76 T. Kosukoglu, M. Carpan, S. Riza Tokgoz and A. Peksoz, Fabrication of a new rGO@PPy/SS composite electrode with high energy storage and long cycling life for potential applications in supercapacitors, *Mater. Sci. Eng., B*, 2022, **286**, 116032, DOI: **10.1016/j.mseb.2022.116032**.

77 L. Jiang, *et al.*, Freestanding rGO/Co_3O_4/PPy Composite Films as Electrodes for Supercapacitors, *Energy Technol.*, 2019, **7**, 1800606, DOI: **10.1002/ente.201800606**.

78 M. S. Anantha, *et al.*, Single step assemble of cerium oxide embellished on layered graphene oxide: an efficacious electrode for supercapacitors and hydrogen evolution reaction, *Mater. Sci. Eng., B*, 2022, **284**, 115924, DOI: **10.1016/j.mseb.2022.115924**.

79 M. V. Arularasu, T. V. Rajendran, B. Arkook, M. Harb and K. Kaviyarasu, Enhanced Electrochemical Performance of Highly Porous CeO_2-Doped Zr Nanoparticles for Supercapacitor Applications, *Microsc. Res. Tech.*, 2025, **88**, 621–630, DOI: **10.1002/jemt.24728**.

80 R. Pitcheri, *et al.*, Effect of Ce-doping on the structural, morphological, and electrochemical features of Co_3O_4 nanoparticles synthesized by solution combustion method for battery-type supercapacitors, *Ceram. Int.*, 2024, **50**, 50504–50515, DOI: **10.1016/j.ceramint.2024.09.396**.

81 A. J. Ramya, G. Raja, M. Raja and A. Subramanian, Effect of conducting polymer-decorated PPy@rGO hybrid electrodes with high specific capacitance and long-term stability for energy storage devices, *Chem. Pap.*, 2023, **77**, 6907–6918, DOI: **10.1007/s11696-023-02985-z**.

82 A. Varghese and K. R. S. Devi, Tailoring a Multifunctional PEDOT/Co_3O_4–CeO_2 Composite for Sustainable Energy Applications, *Adv. Sustain. Syst.*, 2024, **8**, 1–11, DOI: **10.1002/adsu.202300575**.

83 M. G. Hosseini, *et al.*, Fabrication of strontium hexaferrite/reduced expanded graphene oxide/polyaniline ternary hybrids as supercapacitor electrodes, *J. Mater. Sci. Mater. Electron.*, 2025, **36**(617), DOI: **10.1007/s10854-025-14642-0**.

84 D. C. Pawar, D. B. Malavekar, J. H. Kim and C. D. Lokhande, Chemically deposited reduced graphene oxide/polypyrrole (rGO/PPy) composite thin films for flexible solid-state supercapacitor: effect of rGO composition, *Electrochim. Acta*, 2025, **514**, 145671, DOI: **10.1016/j.electacta.2025.145671**.

85 K. Panigrahi, S. Mal and S. Bhattacharyya, Deciphering interfacial charge transfer mechanisms in electrochemical energy systems through impedance spectroscopy, *J. Mater. Chem. A*, 2024, **12**, 14334–14353, DOI: **10.1039/D4TA00537F**.

86 S. Karmakar, Impedance Spectroscopy for Electroceramics and Electrochemical System, *Adv. Energy Convers. Mater.*, 2024, 10–56, DOI: **10.37256/aecm.6120255567**.

87 S. K. Godlaveeti, *et al.*, Synthesis and electrochemical performance of CeO_2/NiS nanocomposite for enhanced asymmetric supercapacitor device applications, *Mater. Sci. Semicond. Process.*, 2024, **184**, 108796, DOI: **10.1016/j.mssp.2024.108796**.

88 M. R. Khawar, *et al.*, Cerium oxide nanosheets-based tertiary composites (CeO_2/ZnO/$ZnWO_4$) for supercapattery application and evaluation of faradic & non-faradic capacitive distribution by using Donn's model, *J. Energy Storage*, 2022, **55**, 105778, DOI: **10.1016/j.est.2022.105778**.

89 N. James, S. Simon, S. Rajeevan, S. C. George and S. P. Balakrishnan, Symmetric Supercapacitors based on Reduced Graphene Oxide/Multi-walled Carbon Nanotubes/Cobalt Oxide Ternary Composites, *J. Macromol. Sci. Part B Phys.*, 2024, **63**, 750–771, DOI: **10.1080/00222348.2023.2285656**.

90 P. Siwach, *et al.*, Nanostructured nickel-doped manganese oxide/polypyrrole/graphitic carbon nitride hydrogel as high-performance supercapacitor electrodes, *FlatChem*, 2024, **48**, 100778, DOI: **10.1016/j.flatc.2024.100778**.

91 B. El-yaqub, M. H. Wahid, Z. Zainal, A. H. Abdullah and W. A. Wan Ab Karim Ghani, Porous carbon foams supported rGO-PPy//rGO for asymmteric supercapacitor device, *Mater. Sci. Eng., B*, 2025, **317**, 118173, DOI: **10.1016/j.mseb.2025.118173**.

92 M. Kaur, P. Chand and H. Anand, Aarti. Fabrication of asymmetric supercapacitor device with $NiCo_2O_4$@reduced graphene oxide nanocomposites, *Electrochim. Acta*, 2024, **507**, 145118, DOI: **10.1016/j.electacta.2024.145118**.

93 U. A. Khan, *et al.*, Cerium-based metal-organic framework-derived composite with reduced graphene oxide as an efficient supercapacitor electrode, *J. Energy Storage*, 2021, **41**, 102999, DOI: **10.1016/j.est.2021.102999**.

94 A. Baby, J. Vigneswaran, S. P. Jose, D. Davis and S. PB, Hybrid architecture of Multiwalled carbon nanotubes/nickel sulphide/polypyrrole electrodes for supercapacitor, *Mater. Today Sustain.*, 2024, **26**, 100727, DOI: **10.1016/j.mtsust.2024.100727**.